

DEEP WIDEBAND SINGLE POINTINGS AND MOSAICS IN RADIO INTERFEROMETRY - HOW ACCURATELY DO WE RECONSTRUCT INTENSITIES AND SPECTRAL INDICES OF FAINT SOURCES?

U. RAU

National Radio Astronomy Observatory, Socorro, NM - 87801, U.S.A.

S. BHATNAGAR

National Radio Astronomy Observatory, Socorro, NM - 87801, U.S.A.

F. N. OWEN

National Radio Astronomy Observatory, Socorro, NM - 87801, U.S.A.

(Dated: Received: 04/09/2016; Accepted: 05/19/2016)

Draft version January 2, 2018

ABSTRACT

Many deep wide-band wide-field radio interferometric surveys are being designed to accurately measure intensities, spectral indices and polarization properties of faint source populations. In this paper we compare various wideband imaging methods to evaluate the accuracy to which intensities and spectral indices of sources close to the confusion limit can be reconstructed. We simulated a wideband single-pointing (C-array, L-Band (1-2GHz)) and 46-pointing mosaic (D-array, C-Band (4-8GHz)) JVLA observation using realistic brightness distribution ranging from $1\mu\text{Jy}$ to 100mJy and time-, frequency-, polarization- and direction-dependent instrumental effects. The main results from these comparisons are (a) errors in the reconstructed intensities and spectral indices are larger for weaker sources even in the absence of simulated noise, (b) errors are systematically lower for joint reconstruction methods (such as MT-MFS) along with A-Projection for accurate primary beam correction, and (c) use of MT-MFS for image reconstruction eliminates Clean-bias (which is present otherwise). Auxiliary tests include solutions for deficiencies of data partitioning methods (e.g. the use of masks to remove clean bias and hybrid methods to remove sidelobes from sources left undeconvolved), the effect of sources not at pixel centers and the consequences of various other numerical approximations within software implementations. This paper also demonstrates the level of detail at which such simulations must be done in order to reflect reality, enable one to systematically identify specific reasons for every trend that is observed and to estimate scientifically defensible imaging performance metrics and the associated computational complexity of the algorithms/analysis procedures.

Subject headings: Techniques: interferometric – Techniques: image processing – Methods: data analysis

1. INTRODUCTION

The recent upgrade of the Very Large Array (VLA) has resulted in a greatly increased imaging sensitivity due to the availability of large instantaneous bandwidths at the receivers and correlator. At least two new dish array telescopes (in particular, ASKAP and MeerKAT) are currently under construction to improve upon the VLA's specifications in terms of instantaneous sky coverage and total collecting area. A considerable amount of observing time has been allotted on all three instruments for large survey projects that need deep and sometimes high dynamic range imaging over fields of view that span one or more primary beams. Desired data products include images and high precision catalogs of source intensity, spectral index, polarized intensity and rotation measure, produced by largely automated imaging pipelines. For these experiments, data sizes range from a few hundred Gigabytes up to a few Terabytes and contain a large number of frequency channels for one or more pointings.

In this imaging regime, traditional algorithms have limits in the achievable dynamic range and accuracy with which weak sources are reconstructed. Narrow-band approxima-

tions of the sky brightness and instrumental effects result in sub-optimal continuum sensitivity and angular resolution. Narrow-field approximations that ignore the time-, frequency-, and polarization dependence of antenna primary beams prevent accurate reconstructions over fields of view larger than the inner part of the primary beam. Mosaics constructed by stitching together images reconstructed separately from each pointing often have a lower imaging fidelity than a joint reconstruction. Despite these drawbacks, there are several science cases for which such accuracies will suffice. Further, all these methods are easy to apply using readily available and stable software and are therefore used regularly.

More recently-developed algorithms that address the above shortcomings also exist. Wide-field imaging algorithms (Cornwell et al. 2003; Bhatnagar et al. 2008) include corrections for instrumental effects such as the w-term and antenna aperture illumination functions. Wide-band imaging algorithms such as Multi-Term Multi-Frequency-Synthesis (MT-MFS) (Rau & Cornwell 2011; Sault & Wieringa 1994) make use of the combined multi-frequency spatial frequency coverage while reconstructing both the sky intensity and spectrum at the same time. Wideband A-Projection (Bhatnagar et al. 2013), a combination of the two methods mentioned above accounts for the frequency dependence of the sky separately from that of the instrument during wideband imaging. Algo-

uruvashi@nrao.edu
The National Radio Astronomy Observatory is a facility of the National Science Foundation operated under cooperative agreement by Associated Universities, Inc.

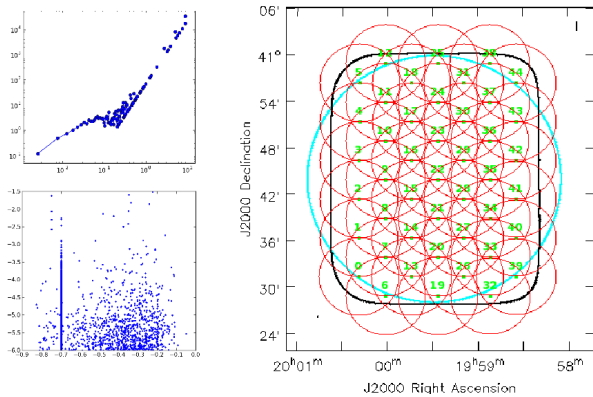


FIG. 1.— Simulated Sky and observations: The top left panel shows the source count vs intensity for 8000 point sources. The bottom left panel shows intensity vs spectral index of these sources. The panel on the right shows the sky coverage of the two simulated observations. The blue circle represents the half-power point of a single pointing primary beam at the VLA L-Band. The red circles represent the individual pointings at C-Band and the black outline shows the half-power level of the mosaic primary beam.

gorithms for joint mosaic reconstruction (Cornwell 1988) add together data from multiple pointings either in the spatial-frequency or image domain and take advantage of the combined spatial-frequency coverage during deconvolution. Such joint mosaic imaging along with a wideband sky model and wideband primary beam correction has recently been demonstrated to work accurately and is currently being commissioned (Rau & Bhatnagar 2014)(in prep). These methods provide superior numerical results compared to traditional methods but they require all the data to be treated together during the reconstruction and need specialized software implementations that are optimized for the large amount of data transport and memory usage involved in each imaging run.

With so many methods to choose from and various trade-offs between numerical accuracy, computational complexity and ease of use, it becomes important to identify the most appropriate approach for a given imaging goal and to quantify the errors that would occur if other methods are used. The Square Kilometre Array (SKA) will involve much larger datasets than the VLA, ASKAP or MeerKAT will encounter with even more stringent accuracy requirements, making it all the more relevant to characterize all our algorithmic options and use existing, smaller instruments to derive and validate algorithmic parameters. This paper describes some preliminary results based on a series of simulated tests of deep wide-band and wide-field mosaic observations with the VLA.

Section 2 describes how the datasets were simulated. Sections 3.1–3.5 list the imaging methods that were compared, for the single pointing as well as the mosaic tests. Section 4 describes the metrics used to quantify imaging quality. Sections 5 and 6 describe the results from several tests performed with the single-pointing and mosaic datasets. Section 7 summarizes the results, discusses what one can and cannot conclude from such tests, and lists several other tests that are required before SKA-level algorithmic accuracy predictions can be made.

2. DATA SIMULATION

A sky model was chosen to contain a set of 8000 point sources spanning one square degree in area. The source list is a subset of that available from the SKADS/SCubed simulated sky project (Wilman et al. 2008). In this sample, intensities ranged between $1\mu Jy$ and $7mJy$ and followed a realistic source count distribution. For high dynamic range tests, one

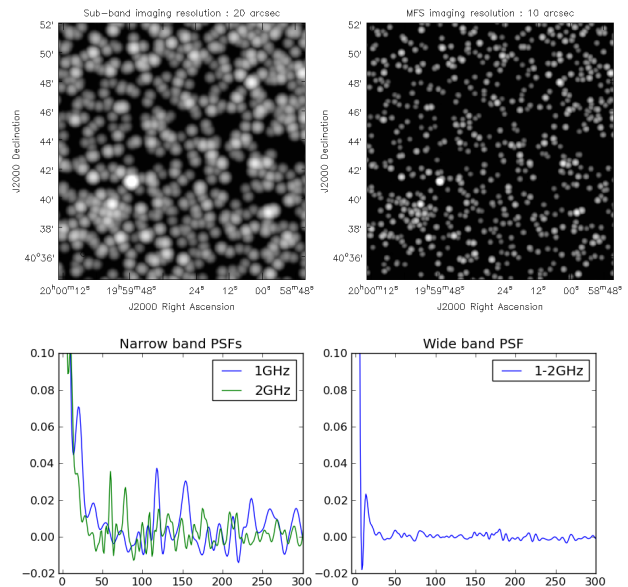


FIG. 2.— Simulated Sky at imaging resolution / PSF sidelobes: A small section of the simulated sky is shown in the top panels, smoothed to 20arcsec (the angular resolution at the low frequency end of the band) in the left panel and 10arcsec (corresponding to the MFS angular resolution) in the right panel. The lower panels show profiles of the inner sidelobes of the PSFs seen by subband and MFS imaging runs. These images and plots illustrate the level of confusion that subband versus MFS based deconvolution algorithms will encounter from the main lobe the PSF as well as its inner sidelobes.

$100mJy$ source was also added. Spectral indices ranged between 0.0 and -0.8 with a peak in the spectral index distribution at -0.7 plus a roughly Gaussian distribution around -0.3 with a width of 0.5. Fig. 1 shows the source count vs intensity on the top-left panel and intensity vs spectral index on the bottom-left¹.

Two types of datasets were simulated. One was for a VLA single pointing at C-config and L-band with 16 channels (or spectral windows) between 1 and 2 GHz. The uv -coverage was a series of snapshots 20 minutes apart, for 4 hours. The HPBW of the primary beam at L-band is 30arcmin and therefore covers the central part of the simulated region of sky. The second dataset was for a VLA mosaic at D-config and C-band with 46 pointings (of primary beams 6arcmin in HPBW) spaced 5 arcmin apart to cover roughly the same patch of sky at a comparable angular resolution. At these simulated angular resolutions (10arcsec at L-band C-config and 9arcsec at C-band D-config), the expected confusion limit is $< 0.5\mu Jy$, and the simulation included only sources brighter than $1\mu Jy$ in order to insulate these tests from errors due to main-lobe confusion. Fig. 2 shows a section of the simulated sky model, smoothed to 20arcsec (the angular resolution at the low frequency end of the band) in the left panel and 10arcsec (corresponding to the angular resolution achieved via Multi-Frequency Synthesis (MFS)) in the right panel. These images illustrate the level of confusion that subband versus MFS based deconvolution algorithms will encounter from the main lobe of the PSF. Sidelobe confusion will add to the complexity of the problem in both cases, but more severely for subband imaging. 16 channels (or spectral windows) were chosen to span the frequency range of 4-8

¹ Such a sharply peaked spectral index distribution is not consistent with observations, it will not affect the conclusions of this papers since the simulations focus on the ability to accurately reconstruct any given intensity and spectral index distribution.

GHz, and the uv -coverage corresponds to one pointing snapshot every 6 minutes, tracing the entire mosaic twice within 8.8 hours.

A true sky image cube was constructed by evaluating wide-band point source components from the SKADS list for a set of frequencies that matched those being observed. All sources were evaluated as delta functions (naturally at pixel centers) using the same cell size as would be later used during imaging. Specific tests with off-pixel-center sources were done by using different image cell sizes during simulation and imaging so that a source at a pixel center during simulation is not at the center during imaging. Visibilities were simulated per pointing for this image cube, using the WB-A-Projection degridded (Bhatnagar et al. 2013) which uses complex antenna aperture illumination functions to model primary beams that scale with frequency, have polarization squint and rotate with time (due to the VLA altitude-azimuth mount).

Noise was not added to these simulations as our first goal was to characterize numerical limits purely due to the algorithms and their software implementations. Only after all observed trends and limits are understood will it be instructive to add Gaussian random noise. Theoretically, pure Gaussian random noise should not change the behaviour of algorithms other than increase error in predictable ways and it is important to systematically confirm that this is indeed the case in practice. However, numerical noise will be present in these tests at the 10^{-7} level as most image domain operations use single float precision. All references to signal-to-noise ratio in this analysis therefore relate to numerical precision noise.

3. IMAGING ALGORITHMS

The datasets described above were imaged in a variety of ways. In all cases the data products were continuum intensity images and spectral index maps. The methods that were tested are several possible combinations of standard CLEAN (Högbom 1974; Schwab & Cotton 1983) for narrow-band imaging, MT-MFS (Rau & Cornwell 2011) for wideband imaging, A-Projection (Bhatnagar et al. 2008) to account for direction-dependent effects during gridding, and stitched versus joint mosaics (Cornwell 1988). Wideband primary beam correction was applied as appropriate using whatever primary beam models were available to the reconstruction algorithms. All image reconstruction runs used the standard major and minor cycle iterative approach (Schwab & Cotton 1983) with different combinations of gridding algorithms for the major cycle (prolate spheroid, A-Projection) and deconvolution algorithms for the minor cycle (Högbom Clean, MT-MFS). The CASA imaging software was used for these simulations and reconstructions as a combination of production tasks and custom C++ code and Python scripts.

3.1. *Cube CLEAN with standard gridding*

Each frequency channel² is reconstructed independently with standard narrow-band imaging algorithms (Clean). There is no intrinsic primary beam correction, but deconvolution is followed by post-deconvolution primary-beam correction done per frequency. All images are then smoothed to the angular resolution of the lowest frequency in the observation, spectral models are fitted per pixel to extract spectral

² In this paper, a reference to frequency or channel implies what is in practice a subband or a collection of data channels that are imaged together using multi-frequency synthesis with the assumption that the spectrum across its width is flat or at least ignorable for the desired imaging dynamic ranges.

indices, and channels are collapsed to form a continuum intensity image.

The main advantage of this method is computational simplicity and ease of parallelization, with each channel and pointing being treated independently. The disadvantage of this approach is low angular resolution and possible sub-optimal imaging fidelity as the reconstruction process cannot take advantage of the additional constraints that multi-frequency measurements provide.

3.2. *Cube CLEAN with narrow-band AWProjection*

This procedure is the same as Cube, but with projection-based gridding algorithms applied per channel to account for baseline and time dependent primary beam effects.

AW-Projection uses models of the antenna aperture illumination functions at different parallactic angles to compute gridding convolution functions per baseline and timestep³. These convolution kernels are constructed to have conjugate phase structure compared to what exists in the visibilities, and this eliminates beam squint during gridding.

The main expected differences from standard Cube imaging is in the quality of the primary beam correction, visible in Stokes V images all the time (beam squint) and at high dynamic range in the Stokes I image.

3.3. *Multi-Term MFS with standard gridding*

Multi-term multi-frequency synthesis was used to simultaneously solve for the sky intensity and spectrum, using the combined wideband uv -coverage. With no intrinsic primary beam corrections, the output spectral Taylor coefficients represent the time-averaged product of the sky and primary beam spectrum $I_v^{sky} P_v$. A wideband post-deconvolution correction⁴ of the average primary beam and its spectrum (P_v) was done at the end to produce intensity and spectral index maps that represent only the sky.

This method has the advantage of algorithmic simplicity while taking advantage of the wideband uv -coverage. The main disadvantage is that the time variability of the antenna primary beam is ignored, which in the case of squinted and rotating beams can result in artifacts and errors in both the intensity and spectrum for sources near the half-power level. Also, since the frequency dependence of the primary beam persists through to the minor cycle modeling stage, the multi-term reconstruction has to model a spectrum that is steeper than just that of the sky. More Taylor terms are required, increasing cost and low SNR instabilities.

3.4. *Multi-Term MFS with wide-band AWProjection*

Multi-term multi-frequency synthesis is used along with Wideband A-Projection Bhatnagar et al. (2013), an adaptation of AW-Projection that uses convolution functions from conjugate frequencies to undo the frequency dependent effects of the aperture function during gridding in addition to accounting for beam rotation and squint. This achieves a clear separation between frequency dependent sky and instrument parameters before the sky intensity and spectrum are modeled. The output spectral Taylor coefficients represent $I_v^{sky} P$ where

³ With an altitude-azimuth mount, the antenna aperture rotates w.r.t to the sky as the antenna tracks a source. The result is a time-variable primary beam where the dominant effect is a rotation related to parallactic angle.

⁴ Post-deconvolution wideband PB-correction is done via [Eq. 14 of REF], a polynomial division carried out in terms of Taylor coefficients.

the effective P is no longer frequency dependent. In this case, a post-deconvolution division of only the intensity image by an average primary beam is required. The output spectrum already represents only that of the sky brightness. Alternatively, a hybrid of cube imaging with narrow-band A-Projection and MT-MFS can also be used in which the frequency dependence of the primary beam is removed in the image domain from the residual image cube before combining the frequency planes to form the Taylor weighted averages needed for the MT-MFS minor cycle. These two approaches have different trade-offs in numerical accuracy, computational load, memory use and ease of parallelization and a choice between them will depend on the particular imaging problem at hand.

This general approach has the advantage of accounting for the time and frequency dependence of the primary beam during gridding, and clearly separating sky parameters from instrumental ones. The required number of Taylor coefficients depend only on the spectrum of the sky, which is usually less steep than that of the primary beam. With A-Projection, a flat-noise normalization choice can sometimes cause numerical instabilities around the nulls of the primary beam where the true sensitivity of the observations is also the lowest – work is in progress to find a robust solution to this. Alternate normalization choices will alleviate the problem but they will increase the degree of approximation that the minor cycle must now handle.

3.5. Wideband Mosaics for Cube CLEAN and MT-MFS

In general, a mosaic can be constructed as a weighted average of single pointing images, using an average primary beam model as the weighting function. In this discussion, a combination after deconvolution will be called stitched mosaic, and a combination before deconvolution will be called a joint mosaic. A joint mosaic can also combine the data in the visibility domain by applying appropriate phase gradients across the gridding convolution functions used by projection algorithms.

Several wideband mosaic imaging options exist (Rau & Bhatnagar 2014) as various combinations of imaging with and without DD correction during imaging, cube versus multi-term multi-frequency synthesis imaging, and stitched versus joint mosaics.

For Cube CLEAN imaging, joint mosaics were made by combining data in the visibility domain and applying appropriate phase gradients across gridding convolution functions. Two methods were compared with the first using an azimuthally symmetric primary beam model to construct a single gridding convolution kernel for all visibilities and the second using full AW-Projection to account for PB-rotation and beam squint (per frequency). The first method has the advantage of computational simplicity compared to full AW-Projection where convolution functions can potentially be different for every visibility, but it has the disadvantage of ignoring beam squint and PB-rotation. The primary beam model is also not the same as what was used to simulate the data and this test evaluates the effect of this commonly used simplification assumption.

For MFS imaging (with multiple Taylor terms), a joint mosaic was computed using AW-Projection with its wideband adaptation (to correct for the PB frequency dependence) along with phase gradients applied to convolution kernels. An alternate approach is to stitch together sets of PB-corrected output Taylor coefficient images, using the time-averaged primary beam as a weighting function, and then recomputing spectral index over the mosaic. However, initial tests showed

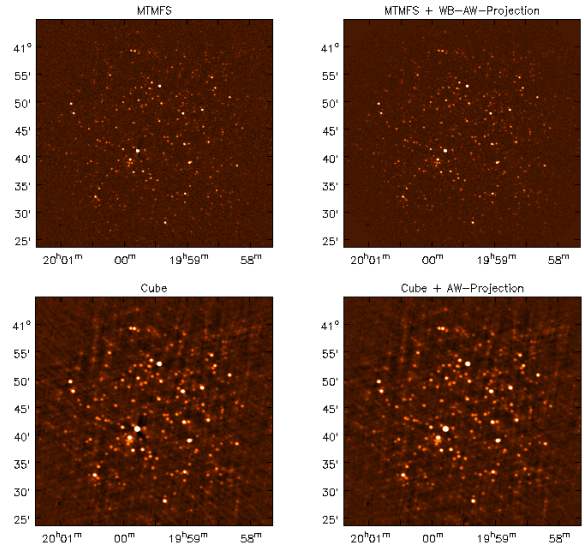


Fig. 3.— Intensity images from the low dynamic range, single pointing tests: The top row shows multi-frequency synthesis (MFS) methods that combine all the data during imaging, the bottom row shows cube methods that treat data from each channel independently, the left column shows imaging with standard gridding in which PB-corrections done only as a post-deconvolution division in the image domain, and the right column uses A-Projection and its wideband variant for more accurate PB correction applied before the sky modeling in the minor cycle.

that stitched mosaics (with or without WB-AWProjection) produced larger errors than joint mosaics (Rau & Bhatnagar 2014) and stitched multi-term MFS mosaics were not included in this analysis.

4. METRICS TO EVALUATE IMAGING ACCURACY

The following metrics were used to evaluate the numerical performance of the different algorithms.

1. Image RMS: The RMS of pixel amplitudes from off-source regions in the image, or in the case of no source-free regions, the width of a pixel amplitude histogram.
2. Dynamic Range: Ratio of peak flux to peak artifact level or image rms when no artifacts are visible.
3. Error distributions (imaging fidelity): The intensity and spectral index maps produced by the above algorithms were compared with the known simulated sky and estimates of error per source were binned into histograms. For each output image, the simulated sky model image was first smoothed to match its angular resolution, and then pixel values were read off from both images at all the locations of the true source pixels. Histograms were plotted for I/I_{true} where deviations from 1.0 indicate relative flux errors and for $\alpha - \alpha_{true}$ where deviations from 0.0 indicate relative errors in spectral index. All histograms were made with multiple intensity ranges (e.g. Fig. 4) and over different fields of view (e.g. Fig. 5) to look for trends.

5. SINGLE POINTING TESTS AND RESULTS

The L-band (1-2GHz) C-configuration simulated data were imaged with the algorithms listed in Sec. 3.1 through 3.4.

5.1. Low-dynamic range algorithm comparison

The first set of tests used a dataset with visibilities recorded as snapshots every 2 minutes, for 4 hours. The resulting

TABLE 1
INTENSITY AND SPECTRAL INDEX RECONSTRUCTION ACCURACY AS A FUNCTION OF SOURCE INTENSITY

Method	I/I_{true}	I/I_{true}	I/I_{true}	$\alpha - \alpha_{true}$	$\alpha - \alpha_{true}$
Intensity Range	$> 50\mu Jy$	$8 - 50\mu Jy$	$< 8\mu Jy$	$> 50\mu Jy$	$8 - 50\mu Jy$
Cube	0.95 ± 0.05	0.9 ± 0.2	0.8 ± 0.3	-0.15 ± 0.2	-0.1 ± 0.3
Cube + AWP	1.0 ± 0.05	0.95 ± 0.2	0.9 ± 0.3	-0.1 ± 0.1	-0.1 ± 0.25
MTMFS	1.0 ± 0.02	1.0 ± 0.05	1.0 ± 0.15	-0.1 ± 0.2	-0.1 ± 0.2
MTMFS + WB-AWP	1.0 ± 0.02	1.0 ± 0.04	1.0 ± 0.15	0.05 ± 0.1	0.05 ± 0.2

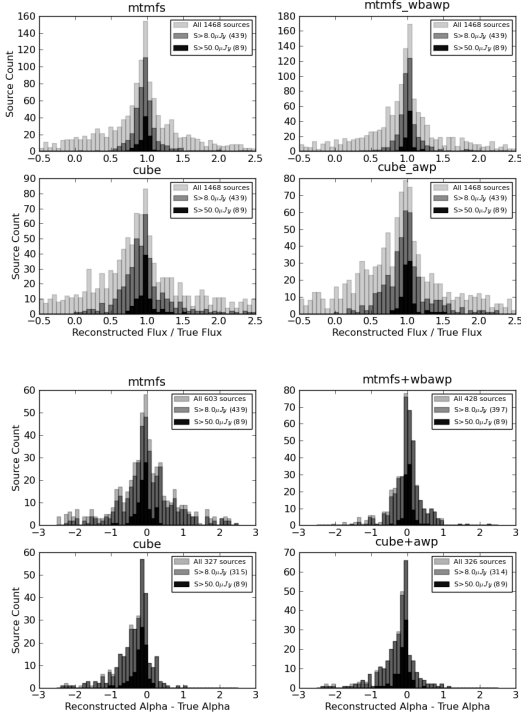


FIG. 4.— Accuracy in Intensity and spectral index as a function of source brightness: The top four histograms show I/I_{true} for the four tested methods and the bottom four histograms show $\alpha - \alpha_{true}$. Each shade represents sources brighter than a certain threshold with darker shades representing higher cutoffs. The increased spread for lighter shades indicates an increase in error for weaker sources.

naturally-weighted PSF had a peak sidelobe level of 0.05 for each channel and 0.02 wideband. The brightest source in this dataset was $7mJy$, chosen to demonstrate the dynamic range limit at which primary beam effects start to show but do not adversely affect surrounding sources. Fig. 3 shows the intensity images from the four methods, with the top row showing multi-frequency synthesis (MFS) methods, the bottom row showing cube methods, the left column with PB-corrections done only post-deconvolution, and the right column with A-Projection for more accurate PB correction.

The first point to note is the difference in angular resolution between the MFS and Cube methods. The width of the restoring beam was $11arcsec$ with MFS and $21arcsec$ with the Cube method. The second is the presence of many undeconvolved sources in the Cube methods, arising from weak sources that go undetected in the single channel reconstructions, but show up only when residual images from all frequencies are stacked. The third is the Y-shaped artifact pattern around the brightest source in the left column. These artifacts are due to PB squint/rotation effects which for the VLA show

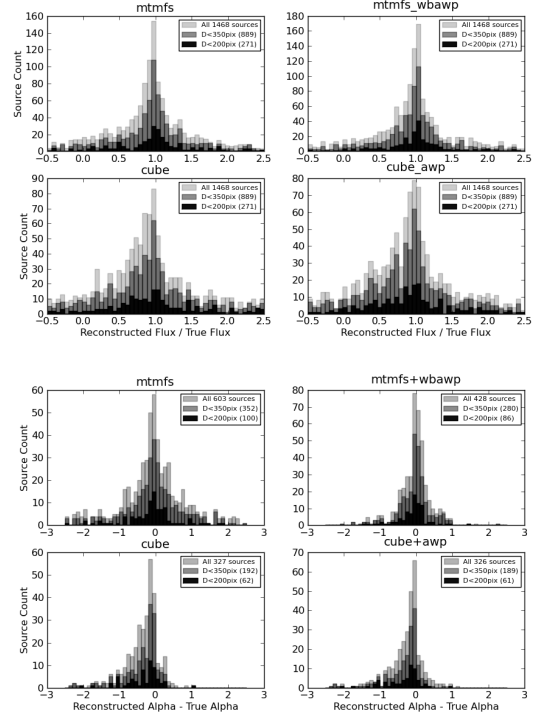


FIG. 5.— Accuracy in Intensity and spectral index as a function of distance from the pointing center: The top four histograms show I/I_{true} for the four tested methods and the bottom four histograms show $\alpha - \alpha_{true}$. The shades represent different maximum distances from the pointing center with darker shades representing the sources closest to the center. Compared to Fig.4, there are no clear trends of source accuracy as a function of location in the primary beam.

up at the ~ 1000 dynamic range level at the 0.7 gain level of each primary beam. The image rms levels $5e-07Jy$ show that upto these dynamic ranges, these artifacts do not contaminate all surrounding sources.

The top 4 panels of Fig. 4 compares I/I_{true} histograms for 1468 sources above $3\mu Jy$ and within the 0.1 gain level of the PB at 1.5GHz. The lower 4 panels show $\alpha - \alpha_{true}$ histograms for all sources that met the threshold for spectral index calculations. The mean and half-width of each of the resulting distributions (over different intensity ranges) for these three methods are listed in Table 2.

The first point to note is a clear widening of the histogram at fluxes $< 10\mu Jy$. Sources brighter than $50\mu Jy$ have errors less than 5%, sources between $50\mu Jy$ and $8\mu Jy$ show errors at the 10% level and sources below $8\mu Jy$ show errors at the 20 to 30% level with several sources more than 50%. MFS imaging (top row) shows slightly lower errors compared to cube imaging especially for weak sources. Cube imaging (bottom row) shows a slight bias towards lower brightness for weaker

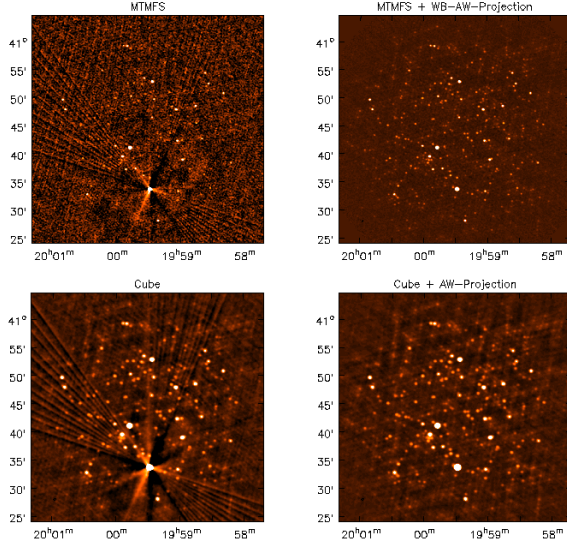


Fig. 6.— Intensity images from the high dynamic range, single pointing tests: The top row shows multi-frequency synthesis (MFS) methods that combine all the data during imaging, the bottom row shows cube methods that treat data from each channel independently, the left column shows imaging with standard gridding in which PB-corrections done only as a post-deconvolution division in the image domain, and the right column uses A-Projection and its wideband variant for more accurate PB correction applied before the sky modeling in the minor cycle. The effect of a bright $100mJy$ source is clearly visible without and with the use of A-Projection.

sources and this is most likely to a residual clean bias effect (see Sec. 5.4) due to the use of single channel PSFs of poorer quality than the MFS PSF.

The trend of brighter sources being more accurate holds for spectral indices as well, but the errors degrade much faster with decreasing source amplitude. Sources brighter than $50\mu Jy$ show errors of ± 0.15 , but sources between $50\mu Jy$ and $8\mu Jy$ show errors of ± 0.5 . In these tests, the weakest sources did not meet the threshold for spectral index calculation and the differences in the number of sources used to compute the displayed histograms reflects this. The spectral indices are slightly more accurate for the MT-MFS imaging along with wideband A-Projection and the only trend worth noting is that the MFS methods produced more sources with usable spectral indices than the cube methods. A faint bias towards steepness for low SNR sources is seen for the cube imaging runs and this could be explained by non-detections at the higher frequencies causing an artificial steepening.

Fig. 5 shows I/I_{true} and $\alpha - \alpha_{true}$ histograms with shades representing distance from the pointing center, out to the 0.2 gain level of the average PB. No obvious trends were noticed, suggesting that primary beam correction is equally accurate everywhere within the 0.2 gain level of the PB. This is expected (and relevant for algorithm validation) as the same aperture illumination model was used for simulation and imaging. In future tests, errors due to the use of approximate models (particularly ones that ignore systematic features) during imaging can be evaluated against these results.

5.2. High-dynamic range algorithm comparison

The above tests were repeated with one additional $100mJy$ source added in. Fig. 6 shows that the only significant change are artifacts characteristic of uncorrected primary beam squint in imaging runs that do not do A-Projection. In this case as seen in Fig. 7, the intensity and spectral index histograms for non A-Projection runs are significantly affected but after cor-

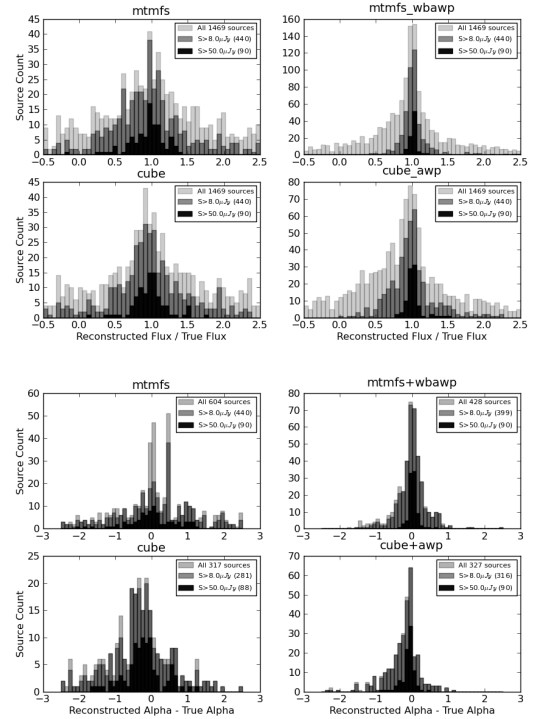


Fig. 7.— Accuracy in Intensity and spectral index as a function of source brightness: The top four histograms show I/I_{true} for the four tested methods and the bottom four histograms show $\alpha - \alpha_{true}$. Each shade represents sources brighter than a certain threshold with darker shades representing higher cutoffs. An increased spread for lighter shades indicates an increase in error for weaker sources.

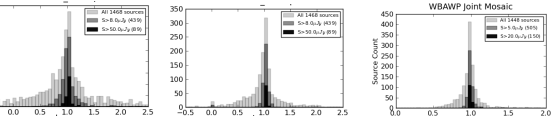


Fig. 8.— Accuracy of intensities as a function of PSF sidelobe level: The three panels (from left to right) show histograms of I/I_{true} when PSF sidelobe levels are 0.05, 0.02 and 0.008 due to different amounts of data. Shades of grey indicate different brightness cutoffs. A lower PSF sidelobe is clearly advantageous for this imaging run of a very crowded field of point sources even if source signal-to-noise is not an issue.

rection are very similar to the low dynamic range example discussed in section 5.1.

5.3. Effect of PSF sidelobe level (and data quantity)

Fig. 8 compares the accuracies of reconstructed source intensities for imaging runs involving different uv -coverages and wideband PSF sidelobe levels. The three PSFs in this test had (from Left to Right) sidelobe levels of 0.05, 0.02 and 0.008. The first PSF is what was used in the low dynamic range simulations described in section 5.1, the second PSF is from a second set of tests with an increased uv filling factor and the right panel shows the PSF from the joint mosaic dataset. These histograms show that as the PSF sidelobe levels decrease, sources brighter than $50\mu Jy$ are always reconstructed to within a few percent. Error on sources in the range $8 - 50\mu Jy$ improve by more than a factor of 4 (from 20% to less than 5%) and by more than a factor of 2.5 on sources in the range $1 - 8\mu Jy$ (from over 50% to $\sim 20\%$). This behaviour is expected even in the absence of noise, simply because of how strongly algorithms like the basic Hogbom Clean minor cycle depend on the quality of the PSF when deconvolving

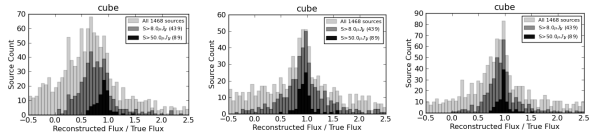


FIG. 9.— Clean Bias: The three panels show histograms of I/I_{true} for three cube imaging runs without masks during deconvolution (left), masks around only the 5 brightest sources (middle) and masks around several tens of sources (right). A systematic downward bias of the reconstructed intensity for weaker sources is known as the clean bias. The use of masks or a PSF with a lower sidelobe level eliminates this problem.

such crowded fields. The fact that errors change significantly even at signal to noise ratios of ~ 300 (sources at $30\mu Jy$ and assuming numerical precision noise at 10^{-7}) shows that PSF sidelobe level is still very relevant. Cube imaging is one practical application where this effect may occur irrespective of noise level, especially if the narrow-band PSFs have higher PSF sidelobes than the joint multi-frequency synthesis PSF. This dependence of accuracy on PSF sidelobe level may be weaker for sparser fields where algorithms such as Hogbom Clean are more robust, but this needs verification (along with the effects of weighting).

5.4. Effect of ‘clean bias’ and use of masks

Clean bias, an effect noticed for decades by users of the Clean algorithm, is a systematic shift of reconstructed peak intensities to lower than expected values. This is usually seen in deep imaging runs with large numbers of closely-spaced weak sources. We did an imaging test using the relatively sparse uv -coverage of 12 VLA snapshots spread across 4 hours and producing a PSF sidelobe level of 0.15. With unaided Hogbom Clean in the minor cycle, a clear shift of intensities to lower values is seen for weaker sources (Left panel of Fig. 9). The use of masks or clean boxes to constrain the search space alleviates the problem (Middle and right panels of Fig. 9). A PSF with lower sidelobes (in our case, the full simulated dataset with MFS imaging) also prevents this type of flux bias with the Clean algorithm and more importantly it does so without having to invoke complicated masking procedures. For example, in our tests, a PSF with sidelobes at 0.13 level showed clean bias but PSFs with sidelobes at the 0.05 level, did not. In cases of high PSF sidelobe levels where clean bias was seen (for example, the narrow band PSFs used for Cube imaging), masks around the 40 brightest sources were sufficient to prevent this bias.

The Clean bias effect can be explained by considering that the Clean algorithm is an L1-norm basis-pursuit method that is optimized for sparse signals that can be described with a minimal number of basis functions. For astronomical images this implies well-separated point sources whose properties can be described by single basis functions (one pixel each) and whose central peaks are minimally affected by PSF sidelobes from neighbouring sources. With 8000 sources within 0.5 square deg, the imaging problem being discussed in this paper is certainly not a sparse signal reconstruction, especially with a PSF with high sidelobes. The Clean algorithm is therefore error-prone in the low SNR regime. A systematic lowering of source brightness can be explained by the algorithm constructing many artificial source components from the sidelobes of real sources.

5.5. Dealing with un-deconvolved sources

With the cube imaging method, the weakest sources are undetected in each narrow band image but appear as un-deconvolved sources when the narrow band restored images are

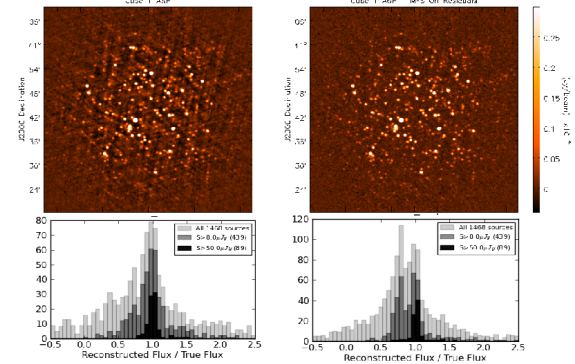


FIG. 10.— Example of a hybrid of MFS and Cube imaging: The left column shows the intensity image after just cube imaging and stacking along with the corresponding I/I_{true} histograms. The right column shows the intensity image and I/I_{true} histograms after the second step of continuum imaging on the residuals.

stacked (seen in the Left panel of Fig. 10). A extra deconvolution step can be done with the continuum residuals, with the assumption that the spectral dependence of weak sources will not cause artifacts. This is almost always guaranteed to be a valid assumption, since at this stage the brightest source is at the narrow-band sensitivity limit, and unless the sensitivity improvement due to bandwidth is more than a factor of 10^3 across a 2:1 bandwidth, residual spectral effects of upto $\alpha = -1$ across a 2:1 bandwidth will not affect the continuum image. The right panel of Fig. 10 shows the resulting image, with a clearly lower background noise level and fewer artifacts. The histograms however show a slight degradation in accuracy with the hybrid method⁵

5.6. Other tests

1. Sources not at pixel centers: Tests were done with sources simulated and imaged using image grids of different cell sizes. Thus, what was at the center of a pixel during simulation, is not at the center during imaging. Slight artifacts were noticed around the brightest sources only beyond a dynamic range of 10^4 but no systematic trends were observed.
2. Increased uv filling factor : To control the computing load of these tests, a relatively sparse uv coverage was used (VLA snapshots taken 20 minutes apart) in the tests described above. The results were later compared with a more realistic uv -coverage constructed from snapshots taken every 2 minutes instead. Errors reduced as expected (as seen in Sec. 5.3) and clean bias was less of an effect but there were no changes in trends between algorithm choices.
3. Numerical effects of different convolution function oversampling ratios: During gridding with A-Projection, convolution functions are computed at a much finer uv resolution compared to the uv -grid onto which the data are being gridded. This is to ensure accuracy when the true uv coordinate is not exactly at the

⁵ The bimodal structure for weaker sources initially appeared to be due to an improper choice of restoring beam size while combining the stacked cube and MFS continuum model images but we have checked that this is not the case. A numerical or software error has not yet been ruled out but we are including this example here to illustrate the types of subtle unexpected effects one may encounter during non-standard usage of even straightforward techniques and software. This is also a source of error and uncertainty that is often ignored in such analyses.

center of an uv grid pixel. Insufficient oversampling of the convolution function results in errors similar to using an inaccurate aperture illumination function model, and effects such as squint and PB rotation are not corrected for accurately enough.

4. Differences between software implementations: In practice, different implementations of the same algorithm may differ slightly in their numerical details, especially as systems become more complex. Some such effects are numerical bugs, but some are simply a result of different choices of normalization and truncation rules. They produce differences at a level comparable to some algorithmic choices and are therefore relevant in such an analysis.

6. WIDEBAND MOSAIC TESTS AND RESULTS

The C-Band mosaic dataset was imaged using three different methods. Fig. 11 shows the resulting restored continuum mosaic images and fig. 12 shows histograms of I/I_{true} and $\alpha - \alpha_{true}$.

The left panel shows the result of cube imaging with a joint mosaic using a different primary beam model than what the data were simulated with and no parallactic angle rotation. In addition to the lower angular resolution typical of cube-based methods, artifacts around the brightest source are clearly visible and the intensity and spectral index histograms show considerable scatter. This test with mismatching PB models between the simulated data and the image reconstruction algorithm was included to illustrate some of the effects of using approximate PBs and algorithmic approximations in practice. The imaging primary beams were defined only by their radial structure and agree with the time averaged true primary beam to within 5% at the half power point. The brightest source in the interior of the mosaic field showing artifacts around it is $1mJy$ in brightness. This image also shows artifacts around sources at the edges of the mosaic, primarily due to the choice of flat noise image normalization that requires a division by the primary beam upto a predetermined cutoff level and the inability of the basic Clean algorithm to handle sources at the very edge of that cutoff level⁶.

The middle panel shows results from A-Projection (using the appropriate PB model) applied per channel as part of a joint mosaic. Artifacts around the brightest source have disappeared because the beam squint and parallactic angle rotation have been accounted for, but as it still is a cube approach, it has limited angular resolution. Similar to the left panel, this also shows artifacts around sources near the edges of the mosaic. The intensity and spectral index accuracy are however improved compared to the left panel, and this is simply because of the more accurate wideband PB model.

The right panel shows the imaging results from joint wideband mosaic imaging with multi-term MFS and wideband A-Projection. The higher angular resolution is immediately apparent and the intensity histogram shows a clear improvement over the other two cube methods. The achieved rms in blank regions within the mosaic field is $0.04\mu Jy$ (in the absence of noise explicitly added to the simulated data). The spectral index histogram also shows a tightening of the errors for bright

sources, but a collection of weak sources appear to have a systematic bias towards steepness. This is clearly an artifact of the algorithm or software. Only some versions of the imaging run (i.e. some choices of parameters and subsets of the data) show this effect and no explanation has yet been found for it. Again, we include this detail in this paper just as a reminder that despite the apparent success of the imaging algorithm as seen from the intensity image (and histogram), numerical surprises may still be lurking in the details and tests at the level of detail that are described here are therefore necessary.

The mean and half-width of each of the resulting distributions (over different intensity ranges) for these three methods are listed in Table 2. Spectral index reconstructions for the weakest sources $< 5\mu Jy$ were not included as all the methods were inaccurate. These numbers show that cube methods have wider distributions for all intensity ranges. This is primarily because of weak sources not detected in single channel images but appear as confused undeconvolved sources in the continuum image. The achieved mean values in both intensity and spectral index show that accurate handling of the primary beam (via A-Projection) is required in order to recover the intensity and spectral index to within a few percent and prevent residual biases, particularly for weak sources.

7. DISCUSSION

The tests described in this paper address the use of wideband data for the deep imaging of crowded fields of compact sources at a sensitivity close to the confusion limit of the observation. The simulations use a realistic source distribution (from which only sources a few times brighter than the confusion limit were used) and include primary beam effects arising from azimuthal asymmetry, parallactic angle rotation and frequency scaling. Noise was not added to these simulations as our primary goal for this paper was to characterize numerical limits purely due to the algorithms and their software implementations. Imaging results were based on the ability to apply appropriate primary beam corrections and recover intensities and spectral indices of sources out to the 0.2 gain level of the primary beam and down to sensitivities a few times the confusion limit. Bright sources were introduced to evaluate dynamic range limits with and without corrections for the time variability of primary beams.

Most observed trends were as expected and we were able to quantify the accuracy with which algorithms performed as a function of source brightness and location in the field of view. There were also a few surprises that highlight the unpredictability of current algorithms in certain situations.

7.1. Algorithm comparisons

We compared multiple algorithms and approaches (for example, traditional versus modern) to understand the limitations of each approach and to decide when the more complicated methods really help⁷.

For a crowded field of compact sources being imaged at a sensitivity close to the confusion limit, the quality of the PSF matters a great deal during deconvolution, and multi-frequency synthesis has a clear advantage over subband based imaging especially for weak sources. The Clean bias effect was seen for Cube based methods which required careful masking to eliminate the effect. However, MFS-based

⁶ An alternate choice of normalization can alleviate this problem but potentially at the cost of not being able to deconvolve as deeply or accurately during the minor cycle and therefore increasing the error in the sky model and amount of computing via extra major cycles..

⁷ Some of these conclusions are at some level a statement of the obvious, but given the folklore that often surrounds such analyses and choices we feel it is worth re-iterating with clear examples.

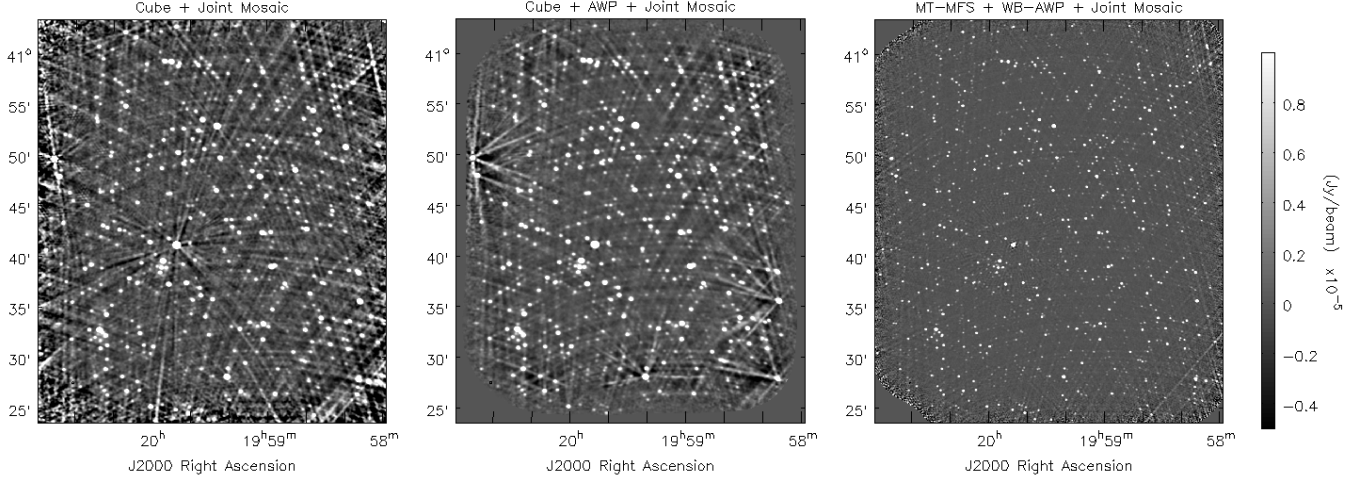


FIG. 11.— Restored continuum intensity images for a wideband mosaic simulation: (LEFT) Cube + Joint Mosaic (narrow band imaging using an approximate form of A-Projection in which the primary beam model is azimuthally symmetric and does not model squint, followed by per channel primary beam correction before stacking to produce a continuum image and spectral fitting), (MIDDLE) Cube + AWP + Joint Mosaic (narrow band imaging using A-Projection that accounts for azimuthally asymmetric primary beam structure and squint, followed by primary beam correction before stacking to produce a continuum image and spectral fitting), (RIGHT) MT-MFS + WB-AWP + Joint Mosaic (wideband A-Projection that corrects for the PB frequency dependence during gridding, combined with the multi-term MFS algorithm with 2 Taylor terms.). The intensity range shown is $-5\mu Jy$ to $+10\mu Jy$ with the rms in blank regions within the mosaic field being $4e-08$ Jy for the right panel.

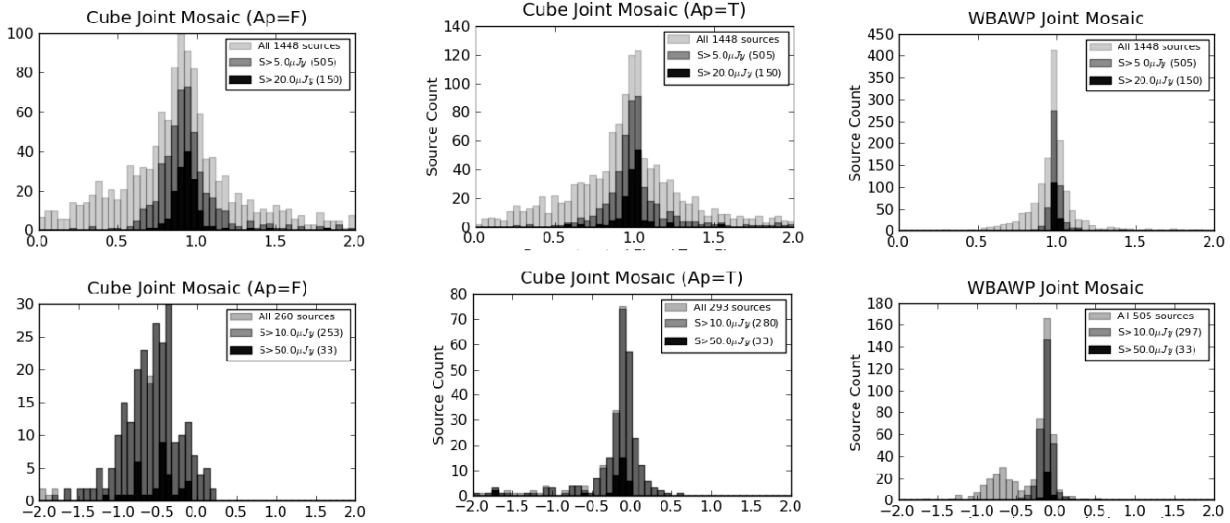


FIG. 12.— Histograms of I/I_{true} and $\alpha - \alpha_{true}$ for the three wideband mosaic images shown in Fig. 11.

wideband algorithms had PSFs with narrower main lobes and lower sidelobes and did not suffer from the clean bias thus making complicated masking procedures unnecessary.

For a mosaic of such a field, a joint imaging approach is preferred (within reasonable image size limits). For dynamic ranges higher than $\sim 10^4$ A-Projection based methods are required to account for baseline and time-dependent primary beam effects. Methods that derive spectral models of the sky while decoupling them from wideband instrumental effects (MT-MFS with wideband A-Projection) are capable of producing usable spectral indices at all SNRs except the lowest SNRs (where all methods fall short). The use of WB A-Projection even at dynamic ranges lower than $\sim 10^4$ might benefit imaging cases where strong sources exist in the outer parts of the PB where PB-spectral index is higher. Finally, simple data parallelization during the major cycle goes a long way in balancing out the increase in cost due to the more complex algorithms.

7.2. Quantifying errors as a function of source brightness

Given the best possible approach (multi-term MFS with wideband A-Projection) for the specific problem being studied (deep widefield imaging of crowded fields at or near the confusion limit), we quantified errors in the recovered intensity and spectral index as a function of source SNR for both single pointings and a joint mosaic. Note that for these noiseless simulations there still is numerical noise at the level of 10^{-7} Jy due to the use of single float precision in many image domain calculations.

For our single pointing tests (at L-Band), errors in reconstructed intensity were as follows. Sources brighter than $50\mu Jy$ have errors less than 5%, sources between $50\mu Jy$ and $8\mu Jy$ show errors at the 10% level and sources below $8\mu Jy$ show errors at the 20 to 30% level with several sources more than 50%. Errors in reconstructed spectral index were as follows. Sources brighter than $50\mu Jy$ show errors of ± 0.15 , but sources between $50\mu Jy$ and $8\mu Jy$ show errors of ± 0.5 . In

TABLE 2
INTENSITY AND SPECTRAL INDEX RECONSTRUCTION ACCURACY AS A FUNCTION OF SOURCE INTENSITY

Method	I/I_{true}	I/I_{true}	I/I_{true}	$\alpha - \alpha_{true}$	$\alpha - \alpha_{true}$
Intensity Range	$> 20\mu Jy$	$5 - 20\mu Jy$	$< 5\mu Jy$	$> 50\mu Jy$	$10 - 50\mu Jy$
Cube	0.9 ± 0.1	0.9 ± 0.3	0.9 ± 0.5	-0.5 ± 0.2	-0.6 ± 0.5
Cube + AWP	1.0 ± 0.05	1.0 ± 0.2	1.0 ± 0.3	-0.15 ± 0.1	-0.1 ± 0.25
MTMFS + WB-AWP	1.0 ± 0.02	1.0 ± 0.04	1.0 ± 0.15	-0.05 ± 0.05	-0.1 ± 0.2

these tests, the weakest sources did not meet the threshold for spectral index calculation (for both cube and multi-term MFS methods).

For such crowded fields, accuracy also depends on the quality of the PSF even if source SNR is not a problem. We showed that as PSF sidelobe levels decreased from 5% to 2% and then 0.8% of the peak (by choosing different subsets of the data) sources brighter than $50\mu Jy$ are always reconstructed to within a few percent, sources between 8 and $50\mu Jy$ improve from 20% errors to less than 5%, and sources between $1\mu Hy$ and $8\mu Jy$ improve from over 50% errors to about 20%.

For our joint mosaic tests (at C-Band), errors in reconstructed intensity were as follows. Sources brighter than $20\mu Jy$ had 2% errors, sources between $20\mu Jy$ and $5\mu Jy$ show errors of 4% and sources below $8\mu Jy$ have about 15% errors. Spectral index errors were ± 0.05 for sources brighter than $50\mu Jy$ but sources between $50\mu Jy$ and $10\mu Jy$ had errors upto ± 0.2 with both cube and MFS methods showing a slight systematic bias of 0.1 towards flatness. The use of an approximate primary beam model (that agreed with the time-averaged ideal beam to within 5% at the half-power level) caused an increase in the error at all brightness levels as well as spurious biases in the reconstructed intensity and spectral index. The difference between the scale of the errors between the single pointing and mosaic tests relate to the amount of data used in the simulation.

7.3. Example of simulation complexity

This study is a demonstration of the level of detail at which such simulations must be carried out in order to begin to be useful as an accurate predictor of reality.

There are many sources of error during image reconstruction and the systematic separation of various contributing factors and their eventual combination is crucial to building a complete picture and truly understanding the reasons behind observed effects. Conclusions derived from approximations done in isolation must be treated with caution and trends observed in real data must be reproduced when applicable. In a first step we include artifacts typical of various instrumental effects (primary beams, PSF sidelobe levels) and demonstrate clean bias and show how to eliminate it. In fact, even the simulations done in this paper require the addition of several more effects to become accurate predictors of reality. For example, this paper quantifies algorithmic limits in the situation of no noise, point sources located at pixel centers, and no differences between the primary beam models used for simulation versus those used during imaging (except for one of the wide-band mosaic tests). These errors are therefore a lower limit on what one could expect in reality. Effects such as the clean bias were reproduced clearly and its cause and solution understood. Future enhancements (even just for Stokes I imaging) should include noise as well as residual calibration errors

(some of which may masquerade as effects needing baseline based calibration), the use of inaccurate primary beam models during imaging, the presence of extended emission in addition to point sources, etc. Such questions are listed in detail in Sec. 7.5.

7.4. Accuracy vs computational cost

Sometimes, algorithmic choices and achievable numerical accuracy depend on the type of available computing resources. This section revisits the various algorithmic options in the context of numerical accuracy versus computational cost.

Cube imaging methods are the easiest to parallelize, with both data and images being partitioned across frequency for the entire iterative imaging process. There is minimal need for special-purpose software for such a setup. Imaging accuracy is limited to that offered by the uv coverage per channel, deconvolution depth is limited to the single channel sensitivity, and the resolution at which spectral structure can be calculated is limited to that of the lowest frequency. There is no dependence on any particular spectral model which makes this approach very flexible in its reconstruction of spectral structure.

Multi-frequency synthesis is demonstrably superior for continuum imaging due to its increased angular resolution, imaging sensitivity and fidelity, especially for crowded fields with thousands of compact sources. The multi-term MFS algorithm is useful to compute in-band spectral indices along with intensity but the cost of both the major and minor cycle increase with the order of the polynomials used. Also, the accuracy of the spectral indices depends on the source SNR⁸ and the choice of the order of the polynomial. Work is in progress to test an approach where the number of Taylor terms is SNR dependent. For multi-frequency synthesis, only the major cycle can be easily parallelized, with a gather step performed before the joint deconvolution step. The preferred partition axis when the WB-AWP algorithm is used is time because of the use of aperture illumination functions from conjugate frequencies during gridding. If narrow-band A-Projection is used to form a cube before primary beam correction and the formation of Taylor weighted averages in the image domain, the partition axis of choice for the major cycle would be frequency.

Projection algorithms are significantly more expensive than the more standard method of using prolate spheroidal functions during gridding, mainly because of the support size of the convolution kernels and the overhead of computing such functions for potentially every visibility. However, the more useful metric is the *total* runtime for imaging and the extra

⁸ Note that the dependence of the spectral index accuracy on SNR is fundamental and not limited to a particular algorithm (e.g. MT-MFS) or procedure (e.g. Cube imaging) used to measure spectral indices.

cost of using projection algorithms can be offset by a comparable reduction in the runtime due to its numerical advantages. For example, WB A-Projection increases the computing load for imaging but decreases the computing load and memory footprint of the MT-MFS setup which will need fewer terms to fit the spectral structure since the primary beam spectrum has been eliminated. Also, in practice the roughly 10 fold increase in computation due to the use of A-Projection compared to the standard gridding is readily absorbed by simple data parallelization during the major cycle. In addition, approximations can always be made (identical antennas, coarser sampling of the aperture illumination function to reduce the size of the convolution functions, etc) but effects of such approximations are visible beyond the $\sim 10^5$ dynamic range level.

Another axis along which parallelization is relatively easy is pointing. However, our tests show that the numerical differences between stitched vs joint mosaics are large enough that (for crowded fields) joint mosaics are always preferred. Another basic factor is the use of single vs double precision calculations during imaging and deconvolution. Currently (in CASA), all intermediate and output images use single precision, which is not the best option for dynamic ranges $\geq 10^7$.

In summary, an appropriate choice of algorithm depends (as always) on the desired angular resolution, imaging sensitivity (and fidelity), dynamic range, data volume and available computing resources.

7.5. Open questions

The simulations and tests described in this paper demonstrate several ways in which imaging accuracy can be sub-optimal even for the simple situation of point sources imaged using both traditional trusted techniques as well as newer ones. A vast number of open questions and details remain, and a truly accurate picture can be derived only after these avenues are explored carefully and quantified to provide trends and usage guidelines to astronomers.

Work is in progress on several of these fronts, and results will be presented in subsequent papers.

1. Is it better to trade integration time at a single frequency band for shorter samples taken across a wider frequency range? For example for the VLA, simulations have shown that comparable imaging sensitivities and far more accurate spectral indices are recovered when an observation spans multiple bands (L-Band and C-Band for example) compared with the entire time spent at only one band.
2. What is the best algorithm for emission consisting of extended structure as well as compact emission? Algorithms like Multiscale CLEAN are usable but relatively more expensive in terms of computing and memory footprint load and require considerable human input. Several newer methods have been shown to produce superior results on their own but do not currently have production-quality optimized implementations that one can use.
3. Does the addition of noise and residual calibration errors change any of the above conclusions? Theoretically, one would not expect the addition of Gaussian random noise to change any results but it will be instructive to understand how robust these algorithms are to various noise levels. Residual calibration errors on the other hand might cause changes that must

be quantified (e.g., see Datta et al. (2009)). To assess how well such effects can be corrected, traditional self-calibration techniques must be compared with more flexible methods such as direction dependent calibration schemes and peeling (for example, SAGE), especially to test their effects on the accuracy of the reconstructed sources.

4. How does baseline based averaging affect the achievable accuracy in the reconstructed intensity and spectral index? A popular mode of data compression is to average time-contiguous visibilities that will all fall on the same uv grid cell during gridding. One concern with such an approach is whether it would prevent the handling of time variability of directional dependent instrumental effects or not. A simple test that achieved a data size reduction of 20% for one of the test datasets showed no noticeable effect with A-Projection imaging out to twice the HPBW of the PB. Additional tests must be done with more practical data compression ratios.
5. How effective is the standard P(D) analyses in predicting source counts below confusion limits? Simulations similar to those described in this paper with sources weaker than $1\mu Jy$ (or an observation with a larger angular resolution) can be used to test the effect of main-lobe confusion for the simulated source count distribution and the accuracy of P(D) analyses on such an image.
6. What type of software implementation and parallelization strategy is the most appropriate for a particular type of survey? In the past few years several new modern imagers have begun to become available and it would be instructive to repeat an imaging test with different algorithms and implementations to evaluate and quantify differences that arise simply from different software implementations and subtle numerical and algorithmic choices within it. For example, Rau & Bhatnagar (2014) shows examples of the numerical differences one can achieve simply by using PB models of different kinds and different algorithmic and software implementations for wideband mosaic imaging.
7. How do these results extend to full polarization imaging and Faraday rotation synthesis? Simulations with polarization dependent primary beams and full-stokes imaging (with and without A-Projection) can quantify polarization imaging limits and identify appropriate imaging strategies. Work is in advanced stages (Jagannathan 2017). to analyse this and produce the required algorithms and software to do such imaging.
8. How accurate do primary beam models need to be for use within A-Projection? Simulations with controlled differences in actual aperture illumination functions can give a useful idea of how much variation can be left unmodeled during imaging. For example, it is easy to produce a spurious bias in spectral index simply by using a PB model whose shape is slightly different from what is present in the data. Work is in progress (Kundert et al. 2016) to quantify imaging errors for ALMA when (not so) subtle differences between antenna structures and illumination patterns are ignored at different levels of approximation and for the VLA (Jagannathan 2017) to carefully model primary beams from holography data and use them during image reconstruction.

7.6. Conclusions

These tests probe the limits of commonly used interferometric imaging algorithms in the context of crowded fields of compact sources being imaged at a few times the confusion limit and > 10 times the (numerical) noise level.

PSF quality with crowded fields : — In this regime, the quality of the PSF is of considerable importance even at signal-to-noise ratios of > 100 simply because of the limitations of Clean based deconvolution algorithms in crowded fields. A PSF sidelobe of $< 1.0\%$ to achieve errors of $< 10\%$ in intensity and < 0.2 in spectral index across a 1-2GHz band for low brightness sources near the confusion limit. Since PSFs from the joint imaging of data (MFS, for example) typically have lower sidelobes compared to PSFs from partitioned pieces of data (Cube, for example) the former are preferred algorithmic choice in this regime.

Clean bias and the need for masks : — Clean bias is a relevant effect in crowded fields when the PSF sidelobe level is high ($> 10\%$ of the peak in our tests). In our tests, Cube methods showed Clean bias and detailed masks were needed to assist the deconvolution algorithms and eliminate the effect. However, MFS-based wideband algorithms had lower PSF sidelobes and did not suffer from the clean bias thus making complicated masking procedures unnecessary.

Sparse fields are easier : — For shallow surveys where the emission above thermal noise limits fills the sky sparsely, we did not find any statistically significant difference between algorithms that partition the data and those that don't (like MFS). Surveys that require imaging at the native resolution of the data/telescope – particularly where detection and reconstruction of extended emission is important – will still need to use MFS. Computing resources will be another discriminator in choosing algorithms in the shallow regime with algorithms that don't require data partitioning (like MFS) requiring fewer resources than algorithms that do require partitioning.

High dynamic range : — For wide-field imaging ($DR > 10^4$), primary beam correction methods need to include details such as its time, frequency and polarization dependence to both reconstruct the bright source accurately and to eliminate artifacts that may contaminate surrounding weaker sources. Our investigation shows that accounting for azimuthal asymmetry of the beams, rotation or pointing jitter as a function of time, scaling with frequency and polarization beam squint due to off-axis feed locations is certainly required.

Errors as a function of algorithm, brightness and location : — With all algorithm combinations we tested on these noiseless simulations, errors on the reconstructed intensity increased from less than 5% for bright sources to $>20\%$ for the weakest micro-Jy level sources. Errors on the spectral index var-

ied from ± 0.15 for bright sources to upto ± 0.5 for the weakest sources and degraded faster than the errors on intensity. Cube based algorithms consistently had slightly larger errors at all intensities compared to MFS based methods. For wide-fields of view, there were no noticeable trends in the errors as a function of distance from the pointing center as long as an accurate wideband primary beam model was used. However, as demonstrated via one of the wideband mosaicing tests, the use of an approximate primary beam model (that agreed with the time-averaged ideal beam to within 5% at the half-power level) can cause spurious biases in both the intensity and spectral index.

Computational load : — The imaging performance of joint image reconstruction methods is fundamentally superior to those that work with partitioned data and combining number of reconstructed images each from a fraction of the available data. Hybrid implementations that take advantage of the ease of parallelization of partitioned methods where possible may be useful, but require careful analysis of its final imaging performance and numerical accuracy. As a general rule, in order to benefit maximally from advanced algorithms, instrumental and sky effects should be separated as early in the image reconstruction process as possible.

Simulation complexity : — Work presented here also gives a lower limit on the level of detail at which simulations for future surveys and telescopes must be undertaken. It is important to systematically build up the complexity of the simulation in a way that enables one to efficiently pinpoint the reasons behind observed feature or trends before moving on and adding more complicating details. Given the wide range of observation types and analysis methods, simulations must be specific to the parameters of each survey and must be as complete as possible in their inclusion of instrumental effects and observing modes. In particular, effects of time, frequency and polarization dependence of the antenna primary beams, effects of long baselines and wide fractional bandwidths, and correct sampling of the coherence field in time and frequency to realistically reflect both the data volume and the filling factor in the uv-plane. Clear accuracy requirements are also necessary for each survey in order to choose the optimal analysis procedure based on scientific estimates.

We wish to thank the various NRAO staff members for useful discussions at various stages of this project. We wish to thank the Common Astronomy Software Applications (CASA) Group for the use of their imaging libraries in our simulation and imaging scripts.

REFERENCES

- Bhatnagar, S., Cornwell, T. J., Golap, K., & Uson, J. M. 2008, *Astron. & Astrophys.*, 487, 419
- Bhatnagar, S., Rau, U., & Golap, K. 2013, *ApJ*, 770, 91
- Condon, J. J., Cotton, W. D., Greisen, E. W., Yin, Q. F., Perley, R. A., Taylor, G. B., & Broderick, J. J. 1998, *Astron. J.*, 115, 1693
- Cornwell, T. J. 1988, *Astron. & Astrophys.*, 202, 316
- Cornwell, T. J., Golap, K., & Bhatnagar, S. 2003, W-Projection: A new algorithm for non-coplanar baselines, Tech. rep., EVLA Memo 67
- Datta, A., Bhatnagar, S., & Carilli, C. L. 2009, *ApJ*, 703, 1851
- Högbom, J. A. 1974, *Astron. & Astrophys. Suppl. Ser.*, 15, 417
- Jagannathan, P. 2017, PhD thesis, University of Cape Town, SA and NRAO, Socorro, USA
- Rau, U., & Bhatnagar, S. 2014, (in prep)
- Rau, U., & Cornwell, T. J. 2011, *aap*, 532, A71
- Sault, R. J., & Wieringa, M. H. 1994, *Astron. & Astrophys. Suppl. Ser.*, 108, 585
- Schwab, F. R., & Cotton, W. D. 1983, *AJ*, 88, 688
- Wilman, R. J., et al. 2008, *mnras*, 388, 1335
- Kundert, K., *IEEE Trans. in Ant.&Prop* (in review)